Raman and coherent anti-Stokes Raman scattering microspectroscopy for biomedical applications

Christoph Krafft
Benjamin Dietzek
Michael Schmitt
Jürgen Popp

SPIE

Raman and coherent anti-Stokes Raman scattering microspectroscopy for biomedical applications

Christoph Krafft,[a] **Benjamin Dietzek,**[a,b] **Michael Schmitt,**[b] **and Jürgen Popp**[a,b]
[a]Institute of Photonic Technology (IPHT) Jena, Albert-Einstein-Straße 9, 07745 Jena, Germany
[b]Institute for Physical Chemistry and Abbe Center of Photonics, Friedrich-Schiller-University Jena, Helmholtzweg 4, 07743 Jena, Germany

Abstract. A tutorial article is presented for the use of linear and nonlinear Raman microspectroscopies in biomedical diagnostics. Coherent anti-Stokes Raman scattering (CARS) is the most frequently applied nonlinear variant of Raman spectroscopy. The basic concepts of Raman and CARS are introduced first, and subsequent biomedical applications of Raman and CARS are described. Raman microspectroscopy is applied to both *in-vivo* and *in-vitro* tissue diagnostics, and the characterization and identification of individual mammalian cells. These applications benefit from the fact that Raman spectra provide specific information on the chemical composition and molecular structure in a label-free and nondestructive manner. Combining the chemical specificity of Raman spectroscopy with the spatial resolution of an optical microscope allows recording hyperspectral images with molecular contrast. We also elaborate on interfacing Raman spectroscopic tools with other technologies such as optical tweezing, microfluidics and fiber optic probes. Thereby, we aim at presenting a guide into one exciting branch of modern biophotonics research. © *2012 Society of Photo-Optical Instrumentation Engineers (SPIE).* [DOI: 10.1117/1.JBO.17.4.040801]

1 Introduction

C.V. Raman was awarded the Nobel Prize in 1930 in recognition of the discovery of inelastic light scattering. In honor of him, spectroscopy on the basis of inelastic vibrational scattering is named Raman spectroscopy. Despite the fact that the Raman effect has been discovered more than 80 years ago, only the advent of lasers in the 1960s boosted the range of applications of vibrational Raman spectroscopy. While the majority of Raman spectroscopic applications originated in physics and chemistry, the last two decades witnessed increasing applications to bioanalytical and biomedical sciences.[1] The combination of Raman spectroscopy with optical microscopy (Raman microspectroscopy) developed into a powerful imaging technique with molecular specificity and lateral resolution down to the subcellular level. Raman microspectroscopic imaging has been applied in biology and medicine[2,3] and even living systems.[4] There are a number of advantages of Raman spectroscopy for biomedical applications such as its noninvasive and label-free nature, high resolution molecular imaging, minimal sample preparation, and compatibility with aqueous solvents.

Despite the enormous potential of Raman microspectroscopy, Raman scattering faces two limitations when applied to biomedical diagnostics. First, Raman images need to be recorded to resolve the inhomogenous distribution of certain features within cells or tissues. The Raman process suffers from weak cross sections due to roughly only one out of 10^3 to 10^6 scattered photons being scattered inelastically. Therefore, the integration time per spectrum is typically so long (seconds) that Raman imaging of extended areas is experimentally slow (minutes to hours). Another limitation is the Stokes-scattered

Raman photons are spectrally red-shifted relative to the incident photons. Consequently, the weak Raman signals are easily overwhelmed by autofluorescence of the sample itself or contaminations that have much larger cross sections. Though fluorescence can be suppressed by using near-infrared (near-IR) excitation light, this procedure further decreases the data acquisition speed as the scattered intensity depends on the forth power of the excitation frequency. Both limitations of Raman scattering—slow imaging and fluorescence background—can be circumvented by use of coherent, nonlinear Raman scattering. Both spontaneous and coherent Raman scattering benefit from near-IR excitation due to deeper penetration into tissue and reduced cell damage that are important properties in the context of biomedical optics.

This tutorial first introduces the basic concepts of the linear vibrational Raman effect. Then, some fundamental characteristics are summarized for the most important coherent nonlinear Raman scattering methodologies that emerged within the last years for rapid chemical imaging of biological samples. Finally, applications in the context of cells, tissues, optical tweezing, microfluidics, and remote sensing using fiber optic probes are described. The descriptions also include some experimental details. As comprehensive reviews have been given elsewhere,[1–8] data from our lab are presented as examples.

2 Vibrational Raman Effect

Vibrational Raman spectroscopy represents one of the most useful tools for obtaining information about the structure and properties of molecules from their vibrational transitions. Polyatomic molecules exhibit a multitude of vibrations. The so called normal modes are particularly interesting for vibrational spectroscopy. In an oscillating system, a normal mode is a

---

Address all correspondence to: Jürgen Popp, Institute of Photonic Technology (IPHT) Jena, Albert-Einstein-Straße 9, 07745 Jena, Germany. Tel: +49 3641206300; Fax: +49 3641206399; E-mail: juergen.popp@ipht-jena.de.

pattern of motion in which certain parts of the molecule move sinusoidally with the same frequency and in phase. A simple way to describe a normal mode vibration is to approximate a chemical bond as a spring holding two atoms together. The vibrational frequency (ω_q) of a normal mode q depends on the effective mass m moved during the vibration and the binding force represented by the spring force constant k of the normal mode. According to quantum theory the vibrational energy is quantized. In other words, every normal mode (q) can be expressed by a quantum harmonic oscillator with an energy of:

$$E_{v_q} = \left(v_q + \frac{1}{2}\right)\hbar\omega_q,\qquad(1)$$

where v_q is the vibrational quantum number of the normal mode q.

The process of Raman scattering can be described in detail using quantum mechanics, in particular second-order perturbation theory. The interested reader is referred to Refs. 5 and 6. A simple classical electromagnetic field description of Raman scattering on molecular vibrations can be used to capture the essence of vibrational Raman spectroscopy.[9,10]

Starting point is the induced dipole moment μ, which originates from the interaction of an incident time-dependent electric field $E = E_0 \cdot \cos(\omega_0 t)$ and the sample characterized by its molecular polarizability (α):

$$\mu = \alpha E.\qquad(2)$$

Thus the molecular polarizability, α, which is physically related to the extent to which the driving field is able to disturb the equilibrium electron density, i.e., the electron configuration in the absence of an external field, presents the proportionality factor between induced dipole moment and external field. Nuclear motions of the molecules will modify the polarizability as the electron density adiabatically adjusts to the instantaneous nuclear geometry of a molecule to minimize the energy of the system. In order to capture the dependence of the polarizability on the nuclear coordinates q (normal modes) along which the molecule oscillates, the polarizability is expanded into a Taylor series. The expansion is performed for small deviations from the equilibrium nuclear geometry $q = 0$:

$$\alpha = \alpha(q) = \alpha_0 + \left(\frac{\partial\alpha}{\partial q}\right)_{q=0} \cdot q + \dots.\qquad(3)$$

The expression given in Eq. (3) depends on the nuclear coordinate q, which oscillates with a characteristic frequency ω_q around $q = 0$ and can be expressed as:

$$q = q_0 \cdot \cos(\omega_q t).\qquad(4)$$

Inserting the electric field, $E = E_0 \cdot \cos(\omega_0 t)$, and Eqs. (3) and (4) into Eq. (2) one obtains:

$$\begin{aligned}
\mu(t) = {} & \alpha_0 \cdot E_0 \cdot \cos(\omega_0 t) \\
& + \frac{1}{2}\left(\frac{\partial\alpha}{\partial q}\right)_{q=0} \cdot q_0 \cdot E_0 \cdot \cos[(\omega_0 - \omega_q)t] \\
& + \frac{1}{2}\left(\frac{\partial\alpha}{\partial q}\right)_{q=0} \cdot q_0 \cdot E_0 \cdot \cos[(\omega_0 + \omega_q)t].
\end{aligned}\qquad(5)$$

This formula already constitutes the conceptual core of Raman scattering as a special case of the general phenomenon

of light scattering. Truncating the Taylor expansion Eq. (3) after the first term ensures that the classical description leads to linear Raman scattering. If higher order terms are taken into account, formulations for higher order Raman scattering processes, e.g., hyper-Raman scattering, can be obtained. From Eq. (5) it is apparent that the induced-dipole moment, which acts as the source term for secondary radiation, i.e., scattered light, oscillates at three distinct frequencies:

1. The first term in Eq. (5), i.e., $\alpha_0 \cdot E_0 \cdot \cos(\omega_0 t)$, oscillates at the same frequency as the incident radiation. Consequently, it constitutes the molecular source for light scattering at this frequency, which is termed elastic light scattering or Rayleigh scattering. This term, which does not contain any information on the nuclear molecular degrees of freedom, is present for any molecule.

2. The time-dependence of the second term in Eq. (5) is determined by the frequency difference of the electric-field oscillation (ω_0) and the molecular normal mode frequency (ω_q). Hence, this term represents the source for scattered radiation, which is red-shifted compared to the incident laser field. Therefore, this term represents inelastic light scattering and more precisely the Stokes scattered light. This term contains information about the geometrical (molecular) structure of the molecular system as reflected by the molecular vibrations (normal modes) q and consequently via its dependence on ω_q.

3. Finally, the third term represents an oscillation with the characteristic frequency $\omega_0 + \omega_q$. Thus, it represents a source for radiation, which has a shorter wavelength compared to the incoming light. This blue-shifted radiation is called anti-Stokes scattering in analogy to Stokes scattering.

As can be seen from this simple classical derivation of the induced dipole moment responsible for Raman scattering, the inelastically scattered light originates from molecular vibrations, for which a nonzero derivative of the electronic polarizability at the equilibrium geometry along the q'th normal coordinate is required, i.e., $(\partial\alpha/\partial q)_{q=0} \neq 0$ This relation between the induced dipole moment and the nonzero derivative of the electronic polarizability at the equilibrium geometry along the q'th normal mode provides an intuitive selection rule for Raman scattering.

Another way of exciting vibrations is IR spectroscopy, that is, the direct absorption of an IR photon with the appropriate energy $\hbar\omega_q$ to directly promote molecules from the vibrational ground state $v_q = 0$ into the first excited vibrational state $v_q = 1$. Both the IR absorption and Stokes-Raman scattering pattern yield vibrational and thus molecular fingerprint information. However, since IR absorption is a one-photon and Raman scattering a two-photon process, both methods are characterized by different selection rules determining if a vibration is Raman-active, IR-active, or both Raman- and IR-active. Therefore, Raman and IR spectroscopy are complementary to some extent. According to Eq. (5), Raman scattering of a molecular vibration can be observed for every frequency ω_q if the polarizability is nonzero. In contrast, an oscillating molecule can only interact with IR radiation and absorb IR radiation if the electrical vector of electromagnetic radiation oscillates with the same frequency

as the molecular dipole moment. In other words a vibration is IR-active if the vibration modulates the molecular dipole moment μ.

The intensity of the Raman-signal can be deduced considering that the molecular origin of the process is the time-dependent induced dipole moment oscillating at the Stokes frequency. Such oscillating dipole constitutes a Hertzian dipole, i.e., an antenna emitting secondary radiation. The observed Raman intensity is proportional to the power emitted by such antenna which can be expressed according to classical electrodynamics as follows:

$$I_{\text{Stokes}} \propto N \cdot \left(\frac{\partial \alpha}{\partial q}\right)^2_{q=0} (\omega_0 - \omega_q)^4 \cdot E_0^2, \qquad (6)$$

where N is the volume density of scattering molecules. This expression reveals the dependence of the scattered intensity, which is detected in a microspectroscopic experiment, on both molecular (derivative of the polarizability with respect to the nuclear coordinates and frequency of the molecular vibration ω_q) and experimental parameters (excitation laser intensity and frequency ω_0). Vibrational modes visible in a Raman spectrum need to be represented by normal modes along which the molecular polarizability changes at the equilibrium geometry. Thus, the gradient of the polarizability determines the Raman scattering intensity.

It should be noted that the classical picture of light-matter interactions outlined above yields an intuitive understanding of the relative wavenumbers apparent in a Raman spectrum. However, the nonquantum mechanical approach has some severe short falls. This can be most obviously illustrated with the example that classical theory does not account for the different intensities observed for Stokes versus anti-Stokes radiation. This is due to the reason that the classical description neglects the quantum mechanical treatment of molecular vibrations. Briefly, the quantum mechanical interpretation of the Raman effect is based on inelastic scattering of photons from vibrating molecules and is classified as a two photon process. Thereby, Stokes-Raman scattering originates from the vibrational ground state ($v_q = 0$) and ends in the first vibrationally excited state ($v_q = 1$) via a transition into a short lived virtual state (state of a photon and a molecule during an infinitesimal time period), while anti-Stokes Raman scattering transfers the molecules from an already populated vibrationally excited level into the vibrational ground state by inelastic scattering. Thus, the intensity ratio Stokes versus anti-Stokes Raman scattering is determined by the population ratio between vibrational ground versus excited state, and thus, at room temperature the ground state is significantly more populated than the vibrationally excited state Stokes Raman scattering exhibits more intensity than anti-Stokes scattering.

3 Relevant Vibrational Modes for Biomedical Applications of Raman Spectroscopy

A nonlinear molecule consisting of N atoms has $3N$-6 normal modes which can be excited independently. The number is reduced to $3N$-5 for linear molecules. It is needless to state that biologically relevant molecules such as lipids, proteins, DNA, RNA, polysaccharides or secondary metabolites are complex molecular structures, which are composed of many atoms. Consequently, the vibrational Raman pattern of each individual biomolecule contains a multitude of bands. But even if the

number of Raman bands is high, valuable information can be obtained from a Raman spectrum as will be shown here. The frequencies of normal modes can be conceptually classified into two general categories: (i) localized motions that involve particular molecular entities (functional groups), and (ii) motions involving a larger, perhaps unique group of atoms that are associated with fingerprint bands. The characteristic Raman band frequencies which are highly localized in a particular functional group move only slightly among different molecules giving an important and useful relationship between Raman spectral features and molecular structures or functional groups. In organic compounds vibrations of functional groups involving CH, NH, and OH are usually highly localized. These vibrations are to be distinguished from fingerprint bands which—if accurately located—can reveal local molecular features and offer chemical specific information. Examples of both categories are given in Table 1 for biomolecules.

Biomolecules are composed of a limited number of subunits, e.g., 20 amino acids are found in proteins and four nucleotides in DNA. As a consequence of the limited number of subunits, Raman spectra of cells or tissues share many similarities, and differences of specific signatures for cell and tissue types are often minute. The identification of individual proteins by their Raman spectra within the complex matrix of a tissue section is usually difficult, in particular for low abundant proteins. Exceptions include proteins that contain a characteristic cofactor, e.g., a heme group in hemoglobin, or a characteristic structure, e.g., triple helix of collagen. For many biomedical applications of Raman (micro-)spectroscopy the knowledge about the overall protein content of a specimen as compared to the lipid or DNA content is relevant. Then, only protein-specific Raman bands need to be analyzed. One of these bands corresponds to the amide-I vibration (at 1620 to 1710 cm^{-1}). The amide-I vibration is dominantly due to $C = O$ vibrations of the peptide group making up the protein backbone. This band is a sensitive marker for backbone geometry of a protein as the frequency of the mode will depend on the coupling between neighboring oscillators, which in turn is influenced by the secondary and tertiary structure. Other protein specific bands are the phenylalanine symmetric stretching vibration at 1004 cm^{-1} or the amide-III vibration (corresponding to the C–N stretching) at 1230 to 1330 cm^{-1}. In the same manner characteristic bands for the identification of DNA, lipids, polysaccharide and secondary metabolites as, e.g., carotenoids, can be identified. Raman spectra of biomolecules are compiled in the literature.[11] Frequencies of Raman-active vibrations referred to in the context of this paper are summarized in Table 1.

The width and relative intensity of the bands are evident from the Raman spectra in the forthcoming figures. Group frequencies include bands of CH_2 and CH_3 near 2900 and 1450 cm^{-1}. Fingerprint frequencies are the band of tryptophan (Trp) near 1550 cm^{-1} and the PO_4 band near 1090 cm^{-1}. The Trp band varies from 1542 to 1557 cm^{-1} as a function of a torsion angle in the range from 60 to 120 deg. The PO_4 band shifts from 1092 to 1100 cm^{-1} upon transition of B-type to A-type DNA conformation. It is important to note that the spectral contributions of all biomolecules overlap in cells and tissues to complex signatures, and most constituents are usually characterized by more than one band.

The OH bonds within the water molecule are polar. The polarizability of polar bonds is lower than of nonpolar bonds. Consequently, Raman scattering of OH bonds is relatively

Table 1 Summary of frequencies of Raman-active vibrations commonly considered in biomedical applications of Raman-microspectroscopy. Positions of fingerprint bands may vary depending on structures, interactions and environments.

Vibration	Frequencies/cm^{-1}	Indicative of ...
OH	3400, 1640	Water
CH_2/CH_3, C-C	2920, 2880, 2850, 1450, 1300, 1128, 1065	Lipids, proteins
Amide I/III	1620 to 1710, 1230 to 1330	Proteins
PO_4	1090 to 1100	Nucleic acids, phospholipids
$N(CH_3)_3$	716, 875	Phosphatidylcholine and sphingomyeline
	608, 700, 1440, 1674	Cholesterol
C = O	1745	Ester group in phospholipids
Triple helix	810, 850, 930, 1240	Collagen
	620, 1004, 1208	Phenylalanine
	642, 830, 850, 1208	Tyrosine
	760, 880, 1010, 1340, 1360, 1550	Tryptophan
	498, 680, 1485, 1575	Guanine
	729, 1304, 1333, 1577	Adenine
	498, 670, 750, 780, 1370, 1666	Thymine
	780, 1256	Cytosine
	852, 931, 1048, 1085, 1127, 1340, 1382	Glycogen
	663, 740, 1250, 1561, 1582, 1620	Heme (denatured)
C = C-H, C = C	1270, 1660, 3050	Nonsaturated fatty acids
	1160, 1530	Carotene
Hydroxyapatite	960	Mineralized tissue

weak and Raman signals of water give relatively low confounding contributions to spectra of biological material. As the permanent dipole moment of OH bonds is modulated during valence and deformation vibrations, water absorbs IR radiation. Due to the high concentration of water molecules in most biological materials, IR absorption is strong. Consequently, penetration of IR radiation (in particular mid-IR near 1600 cm^{-1} and 3400 cm^{-1} corresponding to 6.25 and 2.94 μm, respectively) is only in the range of few micrometers

4 Coherent Raman Scattering

The inelastic scattering process discussed so far has been considered spontaneous in an ensemble of molecules. Individual molecules scatter independently and the scattered light (and the excited modes) exhibits a random mode-to-mode phase relationship. Thus, the spontaneous Raman spectrum observed is a straight forward superposition of the excited vibrations of all molecules interacting with the excitation laser.

In coherent, nonlinear Raman scattering, more than a single laser frequency is incident on the sample. Typically two lasers conventionally termed pump- and Stokes laser with the respective frequencies ω_P and ω_S are used. The joint interaction of these two lasers with the sample coherently drives molecular vibrations, i.e., the phases of oscillations in individual molecules are locked. Such resonant coherent excitation of the molecular ensemble is achieved by tuning the energy difference between ω_P and ω_S to coincide with the frequency (ω_q) of a molecular vibration. Under such conditions individual molecules within the common focus of the pump- and the Stokes laser experience the beat-frequency $\omega_P - \omega_S = \omega_q$, i.e., the frequency of their own intrinsic Raman active vibration ω_q. This molecular vibration is then coherently driven.

Classically, the excitation of coherent molecular vibrations under the influence of the pump- and Stokes laser fields (E_p and E_S) that is the total field strength ($E = E_p + E_S = E_p^0 e^{i(\omega_p t - k_p z)} + E_S^0 e^{i(\omega_S t - k_S z)}$) can be expressed based on a driven, damped harmonic oscillator model.[12] This approach leads to an expression of the amplitude q of the coherent vibrations enforced by the light fields (E_p and E_S):

$$q = \frac{1}{2m}\left(\frac{\partial \alpha}{\partial q}\right)_{q=0} \frac{E_p^0 E_S^0}{\omega_q^2 - (\omega_p - \omega_S)^2 + i\gamma(\omega_p - \omega_S)}$$
$$\times e^{i[(\omega_p - \omega_S)t - (k_p - k_S)z]}, \tag{7}$$

where γ is the damping constant determining the natural line width of the Raman active transition. Equation (7) reveals that the resulting amplitude (q) of the coherently driven vibrations becomes large, if the difference between ω_P and ω_S, i.e., the frequencies of the pump and the Stokes laser, respectively, matches the vibrational frequency ω_q. Furthermore, only Raman active vibrations can be coherently driven since q will vanish for $(\partial \alpha / \partial q)_{q_0} = 0$ [see also Eq. (5)].

Coherent molecular vibrations can generate a nonlinear third order macroscopic polarization which is the source term of coherent Raman scattering. Since the fundamentals of coherent anti-Stokes Raman scattering (CARS) have been developed,[13] CARS has been mostly used for rapid chemical imaging.[4,5,7,8,14] In order to appreciate the imaging character of CARS microscopy, we will start the following section with a brief tutorial

description of the physical principles underlying the CARS process. This description is followed by an introduction into CARS microspectroscopy, or spectral CARS imaging, and stimulated Raman scattering (SRS) microscopy.

4.1 CARS: Introduction

The third order nonlinear polarization producing the CARS signal is created by the interaction of a third laser pulse (which is generally but not necessarily a replica of the pump pulse) with the coherent molecular vibrations excited by the pump- and Stokes pulse. In other words the coherently driven vibrations with an amplitude (q) expressed by Eq. (7) can modulate another light wave (E_p) to induce a nonlinear polarization given by

$$P_{NL} = \varepsilon_0 \frac{N}{2m} \left[\left(\frac{\partial \alpha}{\partial q} \right)_{q=0} \right]^2 \frac{1}{\omega_q^2 - (\omega_p - \omega_S)^2 + i\gamma(\omega_p - \omega_S)} (E_p^0)^2 E_S^0 e^{i[(2\omega_p - \omega_S)t - (2k_p - k_S)z]}$$

$$= \varepsilon_0 \chi^{(3)} E_p^2 \cdot E_S^* \quad \text{with} \quad \chi^{(3)} = \frac{N}{2m} \left[\left(\frac{\partial \alpha}{\partial q} \right)_{q=0} \right]^2 \frac{1}{\omega_q^2 - (\omega_p - \omega_S)^2 + i\gamma(\omega_p - \omega_S)},$$

(8)

where N is the number of oscillators per volume element that experience the displacement (q) under the influence of pump- and Stokes laser, and $\chi^{(3)}$ is the third order, nonlinear susceptibility. It can be seen that this nonlinear polarization, which constitutes the source polarization for the CARS signal, oscillates at the CARS frequency $\omega_{CARS} = 2 \cdot \omega_P - \omega_S$ and is emitted in the phase-matched direction $k_{CARS} = 2 \cdot k_P - k_S$.

The CARS signal intensity can be calculated by employing the nonlinear polarization [Eq. (8)] as the source term within the Maxwell equations and can be expressed as follows:

$$I_{CARS} \propto |\chi^{(3)}|^2 I_p^2 I_S \text{sinc}^2 \left(\frac{\Delta k L}{2} \right),$$

(9)

where L is the interaction length of the lasers with the sample, I_p and I_S are the pump- and Stokes laser intensities and $\Delta k = k_{CARS} - (2k_p - k_S)$ is the phase mismatch. For phase matched conditions, i.e., $\Delta k = 0$, the sinc function and also the CARS intensity is maximized.

To summarize the CARS process involves the interaction of three photons, namely two pump and one Stokes photon, which generate a directed coherent signal emitted at shorter wavelengths than the exciting lasers (i.e., at the anti-Stokes frequency ω_{aS}) whenever the difference frequency between pump- and Stokes hits a Raman resonance ω_q: $\omega_{CARS} = \omega_p + (\omega_p - \omega_S) = \omega_p + \omega_q = \omega_{aS}$. Thus, in comparison to the weak, incoherent and nondirected Raman scattering CARS leads to a spatially

directed signal determined by the CARS wavevector k_{CARS}. Furthermore, the very often occurring and disturbing autofluorescence in spontaneous Stokes-Raman scattering is avoided in CARS where the signal emerges at the anti-Stokes frequency ω_{aS}. Figure 1 compares spontaneous Stokes-Raman scattering and coherent anti-Stokes Raman scattering with the help of the respective energy level diagrams for three different Raman modes.

Despite the advantages of CARS spectroscopy as compared to spontaneous linear Raman spectroscopy, the applicability of CARS is challenged by the fact that the CARS signal is not only generated when the frequency difference between the pump- and Stokes-laser exactly matches a vibrational Raman resonance of the sample. It can be shown, that CARS is intrinsically not background free, i.e., not only the vibrationally resonant imaginary part of the third-order nonlinear susceptibility $\chi^{(3)}$ contributes to the CARS signal generation. The CARS susceptibility $\chi^{(3)}$ shown in Eq. (8), is a complex value. For Raman resonance conditions, that is $\omega_p - \omega_S = \omega_q$, the real part of $\chi^{(3)}$ becomes zero. Thus, the CARS susceptibility and with it the CARS intensity ($I_{CARS} \propto |\chi^{(3)}|^2$) is solely determined by the imaginary part of $\chi^{(3)}$ which is characterized by a Lorentz profile. In other words, for a single Raman resonance q the CARS signal exhibits a Lorentzian lineshape.

In addition to the Raman resonant CARS susceptibility, a nonresonant susceptibility χ_{NR} must also be considered. The nonresonant contribution to the overall CARS susceptibility
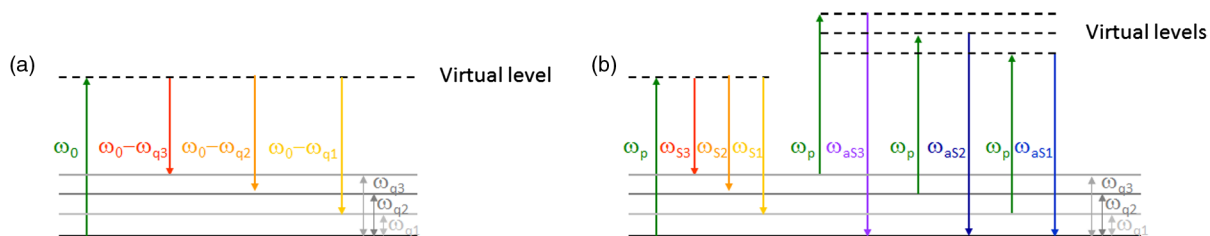

Fig. 1 Schematic display of the energy diagrams relevant for spontaneous Stokes-Raman scattering (a) and CARS (b) for three different Raman modes $q1$, $q2$ and $q3$.

originates from the electronic structure of the medium and is considered to be a real value. The electrons surrounding the nuclei will always oscillate at the difference frequency between pump- and Stokes laser independent of a Raman resonance at $\omega_p - \omega_S = \omega_q$ is fulfilled. Thus, the electrons oscillating at the beat frequency $\omega_p - \omega_S$ will slightly alter the molecules' electronic properties (that is its susceptibility) which is translated into a modulation of the refractive index of the molecules at the beat frequency. From this modulating refractive index grating, a third wave can be scattered off under energy- and momentum conservation generating a directed coherent signal with a frequency of $2\omega_p - \omega_S$. For Raman resonant conditions, the electron cloud becomes more polarizable. Therefore, the electron oscillation amplitude is larger for Raman resonant beating frequencies, i.e., $\omega_p - \omega_S = \omega_q$ resulting in more scattered light under these conditions. Thus, the CARS process consists of two CARS fields namely a nonresonant field due to pure electronic motions and a field due to electron oscillations depending on Raman modes. Both nonresonant and resonant CARS signals are phase matched in the same direction determined by $k_{CARS} = 2 \cdot k_P - k_S$.

Hence, the CARS signal intensity is proportional to the absolute square of the sum of both vibrationally resonant and vibrationally nonresonant parts of the susceptibility. CARS spectra are usually recorded by monitoring the CARS intensity for a fixed pump wavelength while tuning the wavelength of the Stokes laser. The dependency of the square modulus of the overall CARS susceptibility (i.e., resonant and nonresonant contribution) on the detuning δ of the difference frequency between pump- and Stokes frequency from the vibrational Raman frequency $[\delta = \omega_q - (\omega_p - \omega_S)]$ determines the lineshape observed in CARS spectra. Thereby the nonresonant susceptibility χ_{NR} might lead, depending on its magnitude, to asymmetric (dispersive) and complex CARS lineshapes which are very often difficult to interpret. In the case of spectrally overlapping Raman transitions, the observed CARS intensity patterns might be even more complicated because of interference effects between the complex Raman resonant CARS susceptibilities of the nearby Raman transitions and/or interference with the nonresonant background. Thus, even for a small or vanishing nonresonant background CARS line profiles comparable to the ones observed in spontaneous Raman scattering (that is of Lorentzian shape) are only observed for spectrally well separated Raman transitions. For congested spectral regions, interference between the different spectral Raman signatures of the Raman resonant CARS susceptibilities determine the observed CARS line profiles. However, the application of special phase retrieval algorithms, e.g., the maximum entropy method or Kramers-Kronig transformation, can be applied to extract Raman-like information out of the CARS spectra.[15–17]

Despite these limitations, the much stronger signals, as compared to spontaneous Raman scattering, has made CARS into a promising contrast mechanism in optical microscopy for biomedical imaging with high speed within the last ten years.[4,5,7,8,14]

4.2 CARS Microscopy

In the following section, we shall discuss the conceptual strength of combining CARS spectroscopy with laser scanning microscope technology. As already mentioned the resultant technique called CARS-microscopy combines the potential of Raman scattering in recording chemical images of an unstained sample (i.e., the image contrast is based on the vibrational signature of the sample itself) with the benefits of coherent anti-Stokes spectroscopy (i.e., a coherently amplified and directed signal with no disturbance from autofluorescence of the sample). In the preceding section it has been explained that the CARS signal is directed and the direction is determined by the phase-matching condition ($k_{CARS} = 2 \cdot k_P - k_S$). This phase matching condition is trivially fulfilled in gaseous media, in which dispersion does not play a significant role, so that collinear excitation geometry can be used. In contrast the application of CARS spectroscopy in dispersive media, e.g., liquids, requires in general the application of noncollinear phase matching geometries.[9] However, the application of these noncollinear geometries in microscopy is hindered by their complexity.[18–20] Thus, the combination of CARS spectroscopy as a coherent nonlinear optical process, during which phase-matching needs to be fulfilled, with laser-scanning microscopy raises the question, how phase matching can be met in an optically dense medium, e.g., a tissue section. Here, Zumbusch and colleagues[21] showed in their seminal work that CARS microscopy is possible in a collinear optical geometry, i.e., the direction of the k-vectors of pump-, Stokes- and signal-beam coincide, if a microscope objective with a large numerical aperture is used (typically NA $\approx$ 1). Here, the large angle of incidence causes the presence of a Stokes-beam k-vector, k_S, to fulfill phase matching for every vector k_P present in the focus. Furthermore, if this tight-focusing regime is met in CARS microscopy, the CARS signal itself is generated only over a very short interaction length (L) of the incident lasers with the sample. In other words in such a tight-focusing regime, the CARS signal stems from a very constrained spatial volume. The CARS signal can be detected either in the forward (F-CARS) or in backward (EPI-CARS) direction[21–23] Since the interaction length L in the sample is short, all scattering objects lead to large F-CARS signals as the phase mismatch ($[\Delta k = k_{CARS} - (2k_p - k_S)]$) is small [see also Eq. (9)]. This situation is different for EPI-CARS, where for large objects the phase-mismatch is significant. Thus, EPI-CARS signal is only generated from small objects, that is, where L is small enough to develop the sinc function within the expression for the CARS intensity [see Eq. (9)] to the maximum. Though at the first glance this seems to present a severe disadvantage, EPI-CARS can be used experimentally to exclusively monitor small objects embedded in a matrix as introduced by Xie and coworkers.[22] However, it has to be mentioned that for turbid samples, the F-CARS signal might be backscattered to generate an EPI signal.

The CARS-signal generation in a small focal volume offers another benefit of CARS microscopy: the method-intrinsic confocality. As a consequence of this universal feature in nonlinear optical microscopy, in which the signals (e.g., two-photon fluorescence, second-harmonic generation or CARS) are generated dominantly in the region of highest field intensities, CARS microscopy has excellent 3D-sectioning capability.[24]

CARS imaging can be commonly performed in two different ways namely as single-band imaging or CARS microspectroscopy (spectral CARS imaging). Both approaches will be briefly summarized in the following.

4.2.1 Single-band CARS microscopy

Single-band CARS microscopy records as the name implies, univariate images, i.e., the spatial distribution of a single Raman band within the sample being monitored. Such single-band CARS images recorded for one given Raman

shift, can be obtained with video repetition rate.[5] Thereby, much of the information contained in a Raman spectrum is traded off for the capability of rapidly recording images of relatively large tissue sections. Thus, very often single-band CARS microscopy is complemented by spontaneous Raman microspectroscopy in the following way: Raman microspectroscopy offering the benefit of recording a full vibrational spectrum at each sample point but at slow speed (pixel integration times in the order of a second are not uncommon resulting in image acquisition times in the order of hours) is used to define essential spectral regions and markers for tissue classification, for example. Single-band CARS microscopy using different Stokes shifts can then be used for a fast imaging of large areas of these preselected spectral descriptors.[25,26]

However, the chemical selectivity, and thus the quality of such single-band CARS images rely on the Raman activity of the mode to be imaged. As outlined in Sec. 4.1, the raw CARS signal results from the coherent interference of the wanted Raman resonant contribution and the unwanted nonresonant background due to the electronic response of the medium. Furthermore, water which is a major constituent in almost all biological samples leads to rather strong resonant background signals due to its spectrally broad Raman bands. Intrinsically, the presence of such background signals reduces the desired CARS image contrast of an object as characterized by the distribution of the vibrationally resonant imaginary part of the susceptibility. For this reason, background reduction in CARS microscopy is a subject of current research in CARS microscopy. In this context the appropriate choice of laser parameters for CARS microscopy renders the discussion: as CARS is a nonlinear process, high field strengths are beneficial for efficient signal generation. Therefore, it is required to use pulsed lasers. However, a compromise between maximum pulse-peak power and spectral bandwidth has to be taken into account because Raman bands have bandwidths of typically 5 to 10 cm^{-1}. If the spectral width of the laser pulses significantly exceeds the width of the Raman bands, the interaction of the laser pulses with the sample causes strong contributions of the vibrationally nonresonant signal.[8] Thus, the use of picoseconds pulses where the bandwidth of the lasers matches the spectral width of the vibrational transitions is a straight forward approach to keep the background as low as possible or to optimize the ratio between resonant signal (baring chemical contrast) versus nonresonant signal.[8] Overall, several approaches[7] have been suggested to reduce the impact of this nonlinear background and contrast reducing nonresonant CARS signals such as heterodyne CARS (i.e., interferometric mixing),[27,28] polarization sensitive CARS,[29] frequency modulation CARS,[30] application of image-processing approaches,[31] or the application of EPI-CARS to detect exclusively small objects of a size determined by the phase mismatch Δk (see also further above).[22,23]

It needs to be kept in mind that the quality of single-band CARS images depends on: (1) the Raman scattering cross section of the mode to be imaged, (2) that this mode is spectrally distinct, i.e., can be found in a wavenumber silent region to avoid spectral interferences with adjacent Raman modes, and (3) on a high enough molecular density of oscillators featuring this mode. All this is fulfilled for the CH_2 stretch vibration within lipids. Thus, many of the single-band CARS microscopy studies reported so far concentrated on lipid imaging such as lipid uptake or cellular mitoses.[4]

It should be also mentioned that a quantitative analysis of CARS images is rather challenging because of the above mentioned, complicated interplay between the molecular-specific vibrational signal and the nonresonant contribution in the CARS signal generation which makes it difficult to detect each contribution separately. Furthermore, the quantification of analytes is also complicated by the CARS-signal intensity dependence on the square of the molecular concentration N which is a consequence of the dependence of I_{CARS} on $|\chi^{(3)}|^2$ which itself scales linearly with N. Moreover, the concentration dependence of CARS changes from such a quadratic behavior for high concentrations to a linear behavior for low concentration of scattering molecules. This is again a consequence of the coherent mixing of the resonant and nonresonant CARS susceptibility contributions and the proportionality of the CARS signal intensity to the squared modulus of the overall third order CARS susceptibility. Due to these complications the quantification of analytes presents a major challenge in CARS microscopy (see also further below).

4.2.2 *CARS microspectroscopy (spectral CARS imaging)*

The majority of CARS imaging studies reported to date are based on single-band CARS microscopy described above.[5] However, just recently within the last 2 to 3 years, multivariate CARS microspectroscopy approaches are also becoming an attractive bio-imaging tool.[32–37] In these multivariate CARS spectral imaging approaches, a complete CARS spectrum, or a spectrum over a significant wavenumber region, is recorded for each spatial pixel in analogy to spontaneous Raman microspectroscopy but at significantly decreased acquisition times.

The most common method of spectral CARS imaging is realized by broadband or multiplex CARS microscopy.[32–35] Here, the pump pulse has a narrow bandwidth (e.g., picosecond pulse) while the Stokes pulse covers a rather large frequency range (e.g., femtosecond pulse or continuum pulse generated via nonlinear processes). The employment of a broadband Stokes pulse results in a simultaneous coherent excitation of all Raman modes accessible by the spectral bandwidth of the Stokes pulse. This of course leads to the generation of a broad range of anti-Stokes photons whenever the Raman resonance condition is fulfilled, i.e., for every frequency component of the broadband Stokes spectrum whose difference frequency with the narrowband pump pulse matches a Raman transition. Thus, by spectrally dispersing the generated CARS signal with a spectrometer and detecting it with a CCD camera a CARS spectrum is obtained. However, the application of a CCD camera with rather long read out times results in image acquisition times significantly slower than video rate speed achieved for single band imaging. Nevertheless, multiplex CARS imaging is still much faster than what spontaneous Raman microspectroscopy can offer.[32] Another challenge of multiplex CARS microspectroscopy is the investigation of thick and highly scattering tissue samples for which an efficient collection of light by a spectrometer is extremely difficult, if not impossible.[5,14,38]

Spectral CARS images can also be recorded by scanning CARS approaches where the Stokes wavelength is scanned to coherently excite the different Raman resonances one by one and not simultaneously like in the multiplex CARS approach discussed above.[36,37] Such a scanning approach avoids the application of a spectrometer and CCD camera and allows the usage of a fast point detector (e.g., photomultiplier tube). However, rapidly over a broad spectral range tunable narrowband Stokes

light sources are required. The realization and application of such a light source which allows for a sequential coherent excitation of Raman modes at a very high speed by picosecond pulses has recently been reported.[38]

Another method to perform CARS microspectroscopy is referred to as spectral focusing.[39,40] Here, a narrowband excitation is achieved by imprinting an identical chirp onto broadband femtosecond pump- and Stokes pulses. Chirp is the expression for the temporal divergence of the frequency components of a spectrally broad femtosecond pulse because of dispersion. This method allows for focusing the complete pulse energy in a small frequency band because the instantaneous frequency difference between pump- and Stokes pulse ($\omega_p - \omega_S$) stays the same over the whole pulse length. This also leads to the emission of a femtosecond CARS pulse having an identical chirp to pump- and Stokes laser. The selection of a Raman resonance is then achieved by adjusting the time-delay between pump- and Stokes pulse. Overall, the successful realization of the various spectral CARS imaging or CARS microspectroscopy approaches relies to a great extent on the availability of the appropriate laser sources to generate the above mentioned CARS spectroscopy excitation schemes (see also Sec. 5).

At the end, a major aspect when applying CARS microspectroscopy has to be mentioned. As outlined in Sec. 4.1, the collected CARS spectra cannot immediately be translated to quantitative, spontaneous Raman information that is why special off-line CARS spectral processing tools are required. In other words, CARS spectra are much more complicated than spontaneous Raman spectra, and special retrieval algorithms are required to extract the relevant Raman information from the spectral CARS pattern. However, multiplex CARS data processing routines based on, e.g., Kramers-Kronig transformation or maximum entropy method have been developed to quantitatively extract the Raman susceptibility from a measured CARS spectrum.[15–17,32,33]

4.3 SRS Microscopy

Another recently developed coherent Raman scattering technique, with a sensitivity comparable to CARS, is stimulated Raman scattering (SRS) microscopy.[6,41–44] Here, the intensity changes of the Stokes-beam after simultaneous interaction with the pump in the sample are monitored. If the photon energy difference of pump and Stokes is tuned to match a molecular vibration in the sample, stimulated Raman scattering takes place and photons are transferred from the pump to the Stokes beam. This is a consequence of the enforced vibrations (q) [see Eq. (7)] at the difference frequency $\omega_q = \omega_p - \omega_S$ induced by the interaction with the pump- and Stokes fields which can also (along with the CARS polarization) generate a nonlinear polarization oscillating at the Stokes frequency ω_S:

$$P_S^{NL} = N \frac{\left[\left(\frac{\partial \alpha}{\partial q}\right)_{q=0}\right]^2 (E_p^0)^2 E_S^0}{4m[\omega_q^2 - (\omega_p - \omega_S)^2 + i\gamma(\omega_p - \omega_S)]} e^{-i(\omega_S t - k_S z)}.$$

(10)

This polarization has the same wavevector as the Stokes wave and can therefore constructively interfere with the Stokes wave and amplify it. In other words this process can be seen as nonlinear mixing of the Stokes wave with the nonlinear Stokes polarization generated by the coherently driven molecular

oscillators (= optically heterodyned detection scheme). Because of this intrinsic heterodyne detection only the imaginary part of the third-order susceptibility (not the real part) contributes to the signal generation which is why SRS has the significant advantage over CARS; it is free of the nonresonant background. Furthermore, it explains why SRS spectra recorded by measuring the amplification of the Stokes beam as a function of the difference frequency between pump- and Stokes beam are identical to spontaneous Raman spectra where the intensity is also proportional to the imaginary part of the third-order susceptibility. Thus, SRS spectra are exclusively characterized by Raman resonant contributions, since SRS only occurs if $\omega_p - \omega_S$ matches a Raman resonance. Note, SRS can be detected in two different ways: (1) amplification of the Stokes beam which is also called stimulated Raman gain spectroscopy (SRGS) or (2) attenuation of the pump beam (SRS transfers photons from the pump to the Stokes beam) which is called stimulated Raman loss spectroscopy (SRLS). SRLS is a consequence of the destructive interference of the nonlinear polarization oscillating at the pump wavelength (induced by the coherent molecular vibrations) with the pump field.

Furthermore, the linear dependency of the SRS intensity on the concentration (which is also a consequence of the intrinsic heterodyne detection) allows for direct quantification. However, the (small) SRS signal is to be detected on top of the intense Stokes beam making the use of lock-in-technology indispensible. Thus, the conceptually cleaner signal (pure vibrational response of the sample) as compared to CARS (interference between vibrational response and nonresonant background) comes at the expense of a more complicated detection scheme. The CARS signal, which has a different color as compared to the incoming lasers, can be easily separated from them by means of optical filters. Recording SRS spectra by scanning the Stokes wavelength requires picosecond light sources which can be quickly tuned over a broad spectral range. The multiplex CARS microspectroscopy approach applying an imaging spectrometer cannot be easily transferred to multiplex SRS microscopy because of the limited dynamic range of the CCD detector. Furthermore, the occurrence of disturbing interference patterns has been reported.[45] However, broadband SRS microscopy for selectively imaging a particular molecular species within a biological samples has been demonstrated very recently via spectrally tailored SRS.[46]

For an overview of the latest developments of this new microscopy technique based on SRS in bioimaging we refer to an excellent very recent review article (see Ref. 6).

5 Characterization of Tissue: Basic Concepts and Challenges

Generally, more bands are observed in Raman spectra of tissues than in other optical spectra that are obtained from elastic scattering, absorption, or fluorescence in the UV, VIS, and NIR range. In Raman spectroscopy—and also in IR spectroscopy—numerous vibrations can simultaneously be excited for all biomolecules such as proteins, lipids, nucleic acids, and carbohydrates. Therefore, more information about the biochemistry, composition, and molecular structures of the underlying sample may be collected without external labels, with minimal preparation, without damaging the samples, and even under *in vivo* conditions. Among the main challenges are that (i) a fraction of the excitation laser wavelength may be absorbed, and (ii) the excited electronic states may return to the ground

states upon emission of fluorescence. The absorption properties may also induce thermal degradation of the sample. As the Raman scattering cross sections are several magnitudes smaller than fluorescence cross sections, even trace amounts of fluorophores can obscure the weaker Raman bands. Therefore, most applications utilize near-IR lasers for excitation where tissues show minimal absorption. Unfortunately, using near-IR excitation lasers also reduces the sensitivity as the scattering intensities are proportional to the forth power of the excitation frequency, and the quantum efficiency of detection systems decreases. The excitation wavelength near 785 nm is a compromise between sensitivity and autofluorescent background. The intensity of Raman signals can be increased by enhancement effects. The most frequently used effects are resonance Raman scattering (RRS), surface enhanced Raman scattering (SERS) and CARS. In RRS, if the excitation laser is tuned close to the absorption band of a chromophore the vibrations of the chromophore can be amplified by several orders of magnitude. In SERS, if the molecule interacts with surface plasmons of a nano-scale structured metal surface the vibrations will experience significant amplification. For brevity, both methods will not be further described here. In CARS, the enhancement is combined with the absence of single-photon, excited, fluorescent emission because signals are generated at higher frequencies, the anti-Stokes portion of the spectrum. However, CARS suffers from nonresonant background as described in the previous paragraph. We will next introduce instrumental details of Raman and CARS microscopes to acquire images. Then, fundamental principles of supervised and unsupervised multivariate data analyses are described in the context of tissue characterization.

5.1 Raman Spectrometers for Biomedical Applications

Typical state of the art Raman spectrometers for biomedical applications that have been commercially available from several manufacturers for years use a compact diode laser for 785 nm excitation, focus the radiation onto the sample by a microscope objective, collect the scattered light in backscattering geometry, separate the elastically scattered light by a notch or an edge filter, disperse the inelastically scattered light in a grating spectrograph, and detect the spectrum by near-IR optimized CCD detectors. The coupling of a Raman spectrometer with a microscope in combination with a high numerical aperture objective offers two main advantages. First, lateral and axial resolutions are achieved down to the limit of diffraction below 1 μm. Sec maximum sensitivity is obtained because both the photon flux (photon density per area) of the focused laser beam onto the sample is at maximum and the collection efficiency of scattered photons from the sample is at maximum.

Raman imaging combines the spectral and the spatial information. Most Raman images are registered in the point-mapping mode. Here, the laser focus is moved by a scanning mirror, or the sample is moved by a motorized stage to the next position of a predefined grid. The total acquisition time depends on the number of spectra, the exposure time per spectrum, and time for moving the stage. As typical exposure times are seconds per spectrum, total acquisition can last several hours for images composed of thousands of spectra. Raman imaging using laser line illumination has been developed to reduce acquisition time. Here, the spatial data is registered on the detector on a line parallel to the entrance slit of the spectrometer and the spectral

information is dispersed perpendicularly. The other spatial dimension of an image is recorded by scanning in the direction perpendicular to that line. This so-called line-mapping registration mode is faster because only one dimension instead of two dimensions in the point-mapping mode has to be scanned. Another parallel registration approach named wide-field Raman imaging employs intense, global sample illumination. The inelastically scattered light from the sample is projected onto a two-dimensional CCD detector. Most wide-field Raman imaging spectrometers use filters to select the wavelength such as dielectric, acousto-optic tunable and liquid-crystal tunable filters.

5.2 CARS Microscopes for Biomedical Applications

In contrast to Raman microscopy, the first commercial CARS microscopes were very recently introduced by Olympus in 2009 (USA) and Leica Microsystems (Germany) in 2010. However, the majority of the CARS microscopes are in-house assembled setups that share some common principles. Main laser sources to record single-band CARS images are tunable, pulsed titanium sapphire lasers pumped by neodymium-doped yttrium aluminium garnet (Nd:YAG), neodymium-doped yttrium orthovanadate (Nd:YVO$_4$) or glass lasers.[5] A fraction of the laser serves as a Stokes pulse; another fraction is used to pump an optical parametric oscillator (OPO) generating the pump pulse. The tunability of the OPO from 500 to 800 nm allows imaging in the wavenumber region between 500 and 4000 cm^{-1}. A delay line adjusts the accurate spatial and temporal overlap of both pulses. Subsequently, the pulses are fed into a commercial laser scanning microscope that is equipped with photomultiplier tubes for signal detection in forward and backward (EPI) direction. Short pass filters separate the signal from the lasers used for excitation. Typical exposure times are seconds per frame which consists of 512×512 data points. The enhancement by the CARS effect allows reducing the exposure time down to few microseconds per point. The commercially available Leica Microsystems CARS microscopy system is exactly based on this common principle.

Various laser concepts have been employed to perform spectral CARS imaging.[32–37] Scanning CARS spectroscopy is commonly performed by spectrally tuning a narrow-band OPO. Multiplex CARS can be realized by two synchronized titanium sapphire lasers in which one narrowband laser serves as the pump laser while the second laser serves as the Stokes laser and generates broadband pulses.[33,34] To simplify the experimental layout, it is also possible to use one single laser system, which can deliver both a narrowband pump and a broadband Stokes laser.[32,47] The Olympus CARS microscopy system emerged from a similar CARS laser concept based on just a single femtosecond laser system.[39] Here, the laser output was split in two parts in which one part served as pump laser while the other part was used to generate the Stokes laser via specially manufactured nonlinear fibers. The spectral CARS imaging capability was realized via the above mentioned spectral focusing concept. Generally various innovative laser concepts for coherent Raman microscopy have been realized recently mainly concentrating on compact, ideally turn-key, light sources based on all-fiber laser systems.[38,48–50]

5.3 Data Analysis in the Context of Tissue Characterization

The goal of chemometric tools is to extract maximum information from Raman and CARS images. A few principles are given

here. Recent papers give an overview of common algorithms in the context of Raman imaging.[51,52] Stand-alone software packages (http://www.cytospec.com), Matlab-based packages (PLS Toolbox, Eigenvector Research, USA) and a package for programming language R (http://hyperspec.r-forge.r-project .org) offer a collection of algorithms. In chemical or functional group imaging only one parameter (e.g., band intensity) is plotted as a function of the pixel coordinate. As most CARS images are registered for a single anti-Stokes shift, chemical imaging is the method of choice for display. The CARS intensity of the band at 2850 cm^{-1} is shown for a colon tissue section as an example [see Fig. 2(a)]. Highest intensities are found for lipid droplets that are also evident in the photomicrograph [Fig. 2(b)]. Image processing could be applied further to analyze morphological details such as the size distribution of lipid droplets.

The vibrational spectroscopic fingerprint of tissue is composed of overlapping spectral contributions from various biomolecules in a broad wavenumber range. Consequently, Raman images are hyperspectral data sets, and multivariate algorithms are more appropriate for their assessment than chemical or functional group imaging, in which a univariate approach is most appropriate. Multivariate algorithms can be roughly divided into factor methods that extract spectral information, cluster methods for partitioning a data set, and classification methods for modeling group differences. Both factor methods and cluster methods also reduce the dimensionality as the data sets are represented by a small number of vectors or clusters. Different implementations of cluster methods are hierarchical cluster analysis, k-means cluster analysis, and fuzzy C-means cluster analysis. A common feature is that the spectra of the data sets are partitioned into groups or clusters according to their similarity. The segmentation can be "crisp" (implying that a spectrum is assigned to one cluster only) or "soft," meaning that each spectrum can be assigned to more than one cluster with probability values between 1 and 0. False color images can be generated based on the cluster membership assigned to each pixel in the data set, or by plotting the probability values of each cluster. Figure 2(c) shows the membership map of a k-means cluster analysis which has been applied to a Raman image. K-means cluster analysis maximizes the distance between k clusters and minimizes the distance between spectra within each cluster by an iterative algorithm. The biochemical information of each cluster is usually analyzed using the mean cluster spectra. The Raman spectra in Fig. 3 represent the mean spectra of four clusters from the image in Fig. 2(c). The Raman spectra of the lipid droplets show significant differences. According to Table 1, bands in the spectrum corresponding to the red cluster (trace 1) are assigned to droplets composed of cholesterol and phospholipids like phosphatidylcholine. Bands in the spectrum corresponding to the dark red cluster (trace 2) are assigned to droplets composed of triacylglycerides. Bands of nonsaturated fatty acid moieties and proteins are less intense in trace 2 than in trace 1. Spectral contributions of hemoglobin dominate in the spectrum of the olive cluster (trace 3). Typical protein bands are evident in the spectrum of the blue cluster (trace 4) with negligible bands of other components. Similarly, more CARS and Raman images have been compared in other reports.[25,53,54]

Several factor methods have been developed to decompose data sets into a bilinear model of variables. In principal component analysis (PCA), the variables are the eigenvectors and eigenvalues of the data matrix, referred to as loadings and scores. Vertex component analysis (VCA) and N-FINDR are other spectral unmixing algorithms that calculate linear combinations of endmember signatures and a set of abundances. The endmember signatures represent the most dissimilar spectra and can be correlated with spectra of constituents, whereas the loadings are mathematical descriptions of variances within the data set that can both be positive and negative. It has been found that VCA and N-FINDR give chemically more relevant results than PCA.[52] The Raman image of the colon tissue section was also processed by VCA as an example. The abundances are plotted in Fig. 2(d)–2(g). High abundance values in Fig. 2(d) correlate
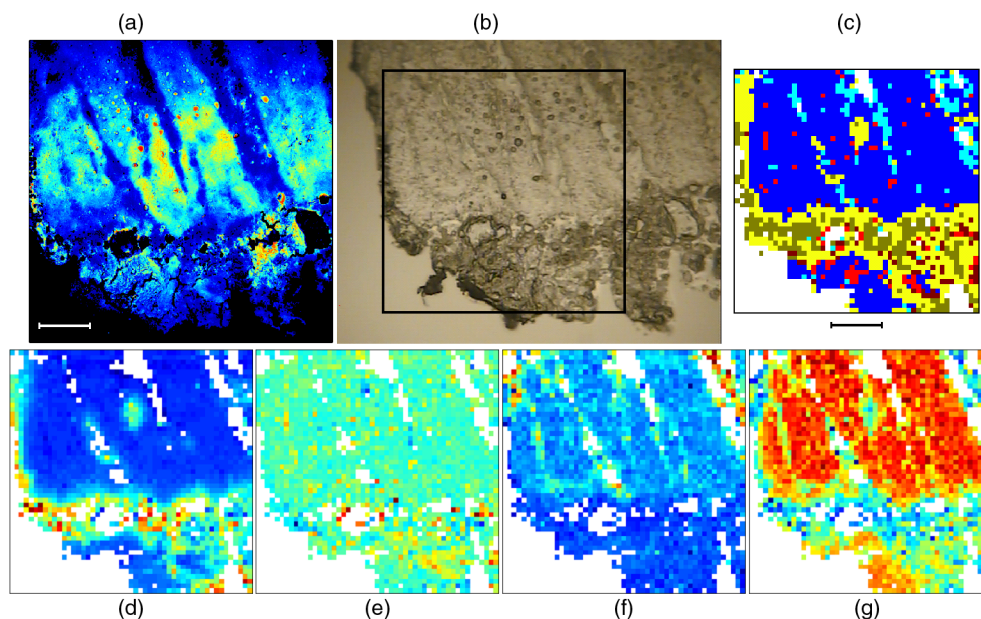

Fig. 2 CARS image (a), photomicrograph (b), and Raman images (c, d, e, f, and g) of colon tissue section. The intensity of the 2850 cm^{-1} is plotted in (a). Box in (b) indicates the region of interest probed by Raman imaging. Color code in cluster membership map (c): colon (blue, cyan), hemorrhage (olive, yellow), lipid droplets (red, dark red). Abundance plots of vertex component analysis: hemoglobin component (d), lipid component (e), collagen component (f) and protein component (g). Color code for abundance from high (red) to low (blue). Bar=100 μm.
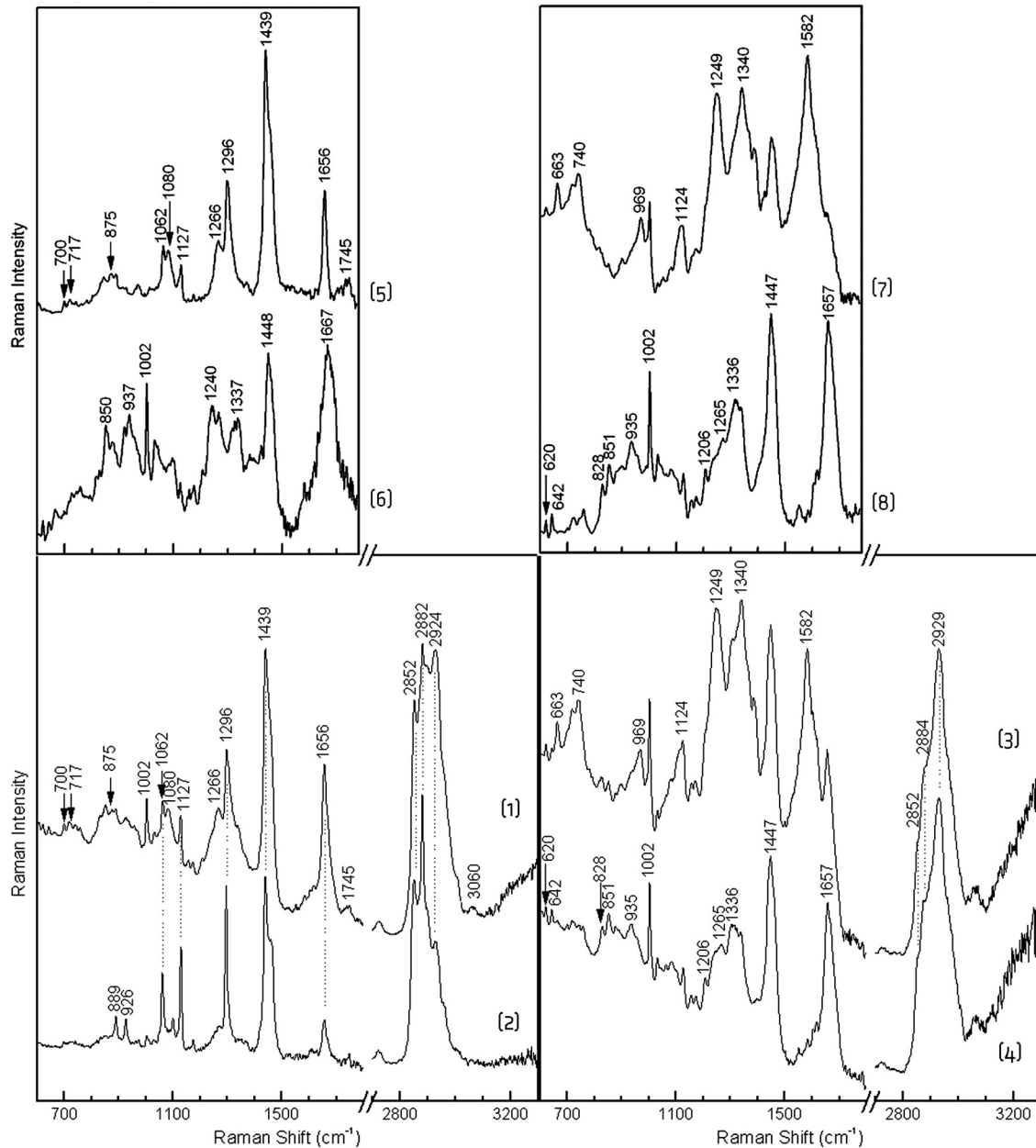
Fig. 3 Raman spectra of lipid droplets and colon tissue from 600 to 3300 cm⁻¹ (traces 1–4) and from 600 to 1800 cm⁻¹ (traces 5–8): droplets composed mainly of cholesterol and phosphatidylcholine (trace 1, red cluster in Fig. 4), droplets composed mainly of triacylglycerides (trace 2, dark red cluster), hemorrhage (trace 3, yellow cluster), and colon (trace 4, blue cluster). Endmember signatures of vertex component analysis of lipid component (trace 5, Fig. 2(e)), collagen component (trace 6, Fig. 2(f)), hemoglobin component (trace 7, Fig. 2(d), and protein component (trace 8, Fig. 2(g)). For clarity, lipid bands are labeled in traces 1, 2, and 5, hemoglobin bands in traces 3 and 7, and protein bands in traces 4, 6, and 8.

with hemoglobin [yellow and olive clusters in Fig. 2(c)], high abundance values in Fig. 2(e) with lipid droplets [red and brown clusters in Fig. 2(c)], and high abundance values in Fig. 2(g) with proteins [blue cluster in Fig. 2(c)]. The endmember signatures of VCA are included in Fig. 3. The lipid component (trace 5) contains almost no spectral contributions from proteins as evident from the missing band near 1002 cm⁻¹. Compared with the cluster mean spectrum (trace 3), the hemoglobin component (trace 7) contains less spectral contributions of proteins as evident from less intense bands near 1002, 1447, and 1657 cm⁻¹ relative to heme-associated bands near 1249, 1340, and 1582 cm⁻¹. The protein component (trace 8) is similar to the cluster mean spectrum of proteins (trace 4) except for the

baseline slope. Instead of triacylglycerides, the forth component is assigned to the protein collagen (trace 6). Collagen can be distinguished from other proteins due to its composition with higher abundances of proline, hydroxyproline, and glycine and the secondary structure elements triple helices. These properties are associated with more intense bands at 850 and 937 cm⁻¹ and band shifts to 1240 and 1667 cm⁻¹. Highest collagen abundances are found in the upper right portion of the Raman image [Fig. 2(f)].

Classification methods use reference knowledge, i.e., class membership of training spectra. Each class is described by a model. The accuracy of classification models is determined by validation procedures. Leave-one-out validation means that

one spectrum is removed from the data set, the classifications models are trained by the remaining spectra, and the missing spectrum is assigned. This procedure is repeated for each spectrum. Subsequently, these models can assign unknown spectra to the predefined classes. The concept can be applied to single spectra of individual samples and spectroscopic images composed of multiple spectra. In the latter case, the resulting class memberships are represented by colors, and color-coded images are assembled for visualization. Linear discriminant analysis (LDA) and support vector machines (SVM) belong to frequently applied classification methods in the context of vibrational spectroscopy. Briefly, LDA calculates $k - 1$ discriminant functions that optimally discriminate k classes. The discriminant functions describe a separation hyperplane. The normal vector of this separation plane is the direction that maximizes the ratio of the difference between classes (inter-class variance) to the differences within the classes (intra-class variance). Similarly, SVM constructs a hyperplane or set of hyperplanes in a high dimensional space which can be used for classification. SVM chooses a so-called maximum margin hyperplane so that the distance from it to the nearest point on each side is maximized. In contrast to LDA, SVM can also model nonlinear class boundaries.

6 Looking Inside: Raman and CARS Fiber Optic Probes

Optical tools for *in-vivo* diagnostics are needed as to guide surgical interventions, to delineate lesion margins or to replace random biopsies of suspicious tissues by targeted biopsies which, in turn, would reduce pathology costs and biopsy-associated risks. Several probe geometries have been designed for use with Raman spectrometers. They can be roughly divided into handheld probes and miniaturized probes for minimal-invasive endoscopic applications. Three probe geometries are depicted in Fig. 4. Generally, laser radiation is coupled into an excitation fiber; the scattering radiation is coupled into a collection fiber, the elastic scattered photons are suppressed by long pass or notch filters; and the inelastic scattered photons are dispersed in a spectrograph and subsequently registered by a CCD detector. The simplest geometry uses the same fiber for excitation and collection [Fig. 4(a)]. Advantages include the low cost and small diameter. Beamsplitter, filter, mirror, and the lens for fiber coupling can be realized in free space optics. One disadvantage is that Raman signals are generated in the fiber core themselves. If silica is used for the fiber core, intense signals will be generated
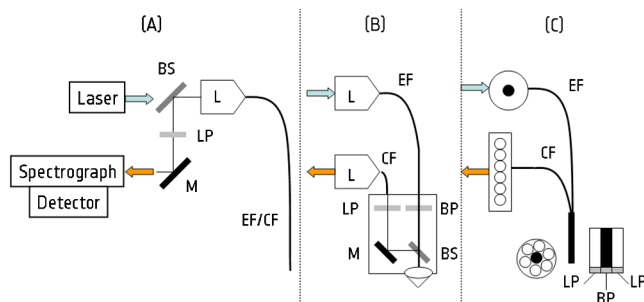
below 1500 cm^{-1} and only the high wavenumber range from 2000 to 4000 cm^{-1}, is accessible.[55] Another disadvantage is the divergence of the radiation at the fiber exit. This can be circumvented by lens-based systems. The second design [Fig. 4(b)] uses a lens to focus the radiation onto the sample and collect the scattered radiation which offers better sensitivity. Here, the excitation fiber is directly coupled to the laser and the collection fiber to the spectrograph. A bandpass filter suppresses the Raman signals of the excitation fiber. A small tube or compact case also incorporates a beamsplitter, lens, mirror, long pass filter and fiber coupling optics. The filtered probe is able to assess the full wavenumber range from 300 to 4000 cm^{-1}. Such a probe has been applied to locate brain tumors in a living mouse by Raman imaging.[56] For further miniaturization, the filters are placed directly onto the fiber ends [Fig. 4(c)]. A bundle of fibers that surrounds the central excitation fiber improves the collection efficiency. The collection fibers are arranged in a line at the entrance slit of the spectrograph. After such probes were introduced in 1999[57] several groups demonstrated their use in model studies.[58,59] Further probe designs and their applications have recently been summarized.[1]

The challenges for CARS probes are to conserve the spatial and temporal overlap of the pump and the Stokes pulse during propagation through fiber, to scan the pulses rapidly over the region of interest, and to efficiently collect the backward scattered signal. An important design consideration is the suppression of optical nonlinearities in the delivery fiber. A step toward such probes is a CARS miniaturized microscope that was designed for imaging of spinal cords in living animals.[60] A biaxial microelectromechanical system (MEMS) mirror was used for scanning, and the CARS signal was generated applying a miniaturized objective. The design also includes a large mode area photonic crystal fiber for light delivery and multi-mode fiber for collection of the nonlinear optical signal. CARS endoscopy was demonstrated utilizing a single mode optical fiber with a focusing unit attached to the distal end.[61] Picosecond pump and Stokes pulse trains were delivered through the fiber with nearly unaltered spectral and temporal characteristics. CARS endoscopic images were recorded by collecting the epi-CARS signal generated at the sample and raster scanning the sample with respect to the fiber. Another fiber delivered probe was introduced for efficient CARS imaging of tissues.[62] This probe used a scanning mirror for imaging. A coherent Raman endoscope that provides stimulated Raman scattering (SRS) images at seven frames per second was described.[63] The device uses a miniaturized fiber scanner, a custom-designed objective lens, and an optimized scheme for collection of scattered light from tissue.

7 Trap, Drag and Measure: Biophysics of Individual Mammalian Cells

An increasing number of papers demonstrated applications of Raman and CARS microscopy to study single cells at the subcellular level.[1,64] Most studies reported data of adherent cells on slides after fixation, in a dried state or surrounded by buffer. Examples are given in Fig. 5. In Fig. 5(a), a Raman image from a single macrophage cell was processed by vertex component analysis. The results are displayed in a red-green-blue composite image highlighting the nucleoli within the nucleus (blue channel), and lipid droplets (red channel) within the cytoplasm (green channel). The Raman spectrum of nucleoli shows spectral contributions of nucleic acids that are labeled according to

Fig. 4 Geometries of Raman fiber sensors: unfiltered single fiber (a), two fibers with filters and lens (b), and fiber bundles with on-the-tip filters (c). Abbreviations: beamsplitter (BS), longpass (LP), mirror (M), fiber coupling lens (L), excitation fiber (EF), collection fiber (CF) and bandpass (BP).

Table 1 [Fig. 5(d)]. The Raman spectrum of the cytoplasm resembles the Raman signature of proteins in tissue (Fig. 3, trace 4). The Raman spectrum of the lipid droplets is similar to the lipid droplets in colon tissue (Fig. 3, trace 1). Although Raman spectra are diagnostic of different lipids[65] assessing the lipid distribution in a droplet and monitoring the specific uptake are complicated due to minute spectral variations and low abundances of some lipids. Deuterium which replaces hydrogen in fatty acid chains can be used to label specific lipids and improve the sensitivity. The Raman image in Fig. 5(b) shows the distribution of deuterated stearic acid (red) in lipid droplets of a macrophage. The nondeuterated cell components are colored cyan. The C-D stretch vibration bands are shifted to lower wavenumbers near 2100 cm^{-1}. If the Stokes laser is set such that the frequency difference with the pump laser equals this frequency the deuterated lipid droplets can also be visualized in CARS images [Fig. 5(c)—see Refs. 4 and 66]. Deuterated lipid droplets are found throughout the cytoplasm, but not in the cell nucleus. A macrophage fully packed with lipids as shown in Fig. 5(c) is called foam cell.

Nonadherent cells, e.g., cells from body fluids such as blood, urine or saliva, can be studied utilizing the optical tweezers effect which is based on the gradient force of a highly focused laser beam. The principle of optical tweezers is that the narrowest point of the focused beam, known as the beam waist, contains a very strong electric field gradient. It turns out that dielectric particles such as cells are attracted along the gradient to the region of the strongest electric field, which is the center of the beam. Raman spectroscopy and optical tweezers are two compatible techniques as the highly focused trapping beam provides the necessary power for Raman excitation while simultaneously providing trapping of a single microparticle. The backscattered signal can be collected by the same microscope objective. Restrictions of single beam optical tweezers include the inability to hold and move larger cells at will, and the tightly focused laser beam may result in undesirable light-induced cell damage, e.g., due to two-photon absorption. Therefore, a dual beam fiber optic trap was developed as another approach to hold and maneuver cells for the recording of Raman spectra. Such a dual beam trap offers the following advantages over the single beam optical tweezers. First, the trap does not require high numerical aperture optics and can be realized with weakly focused or divergent beams. Second, the trap can hold larger objects readily due to the larger catchment area and beam divergence. Third, if the optical trap is realized with fiber lasers it may be readily incorporated into a microfluidic flow system for cell analysis. In general, these approaches have high potential for *in vivo* studies including Raman activated cell sorting as a complement to the well established fluorescence activated cell sorting.[67] Due to the signal enhancement, higher throughput can be expected for microfluidic CARS cytometry.[68] This principle has been demonstrated to measure the population of adipocytes isolated from mouse fat tissues.

8 Comparison of CARS and Spontaneous Raman Microspectroscopy

Typical selling points for CARS microscopy are (1) endogenous, molecularly specific contrast, (2) orders of magnitude higher signals under appropriate experimental conditions, and (3) optical sectioning and 3D imaging due to the inherent localization of the signal and the multiphoton nature of CARS. For biological imaging, higher CARS signals may permit faster acquisition
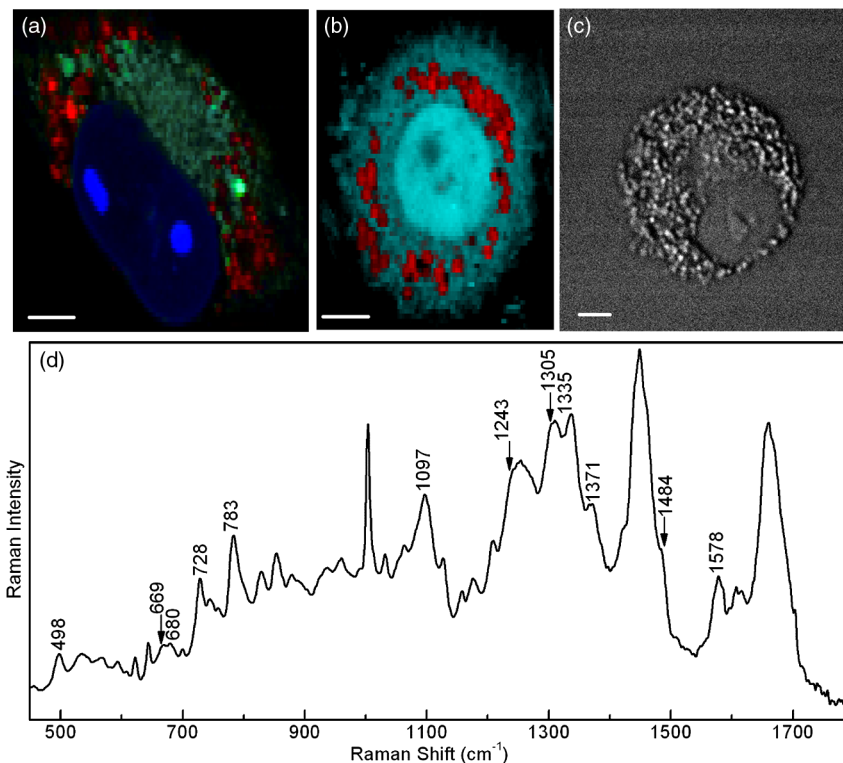

Fig. 5 Raman and CARS microscopic images of macrophages. (a) Vertex component analysis (VCA) of Raman image highlights nucleus (blue channel), cytoplasm (green channel) and lipid droplets (red channel). (b) VCA of another Raman image reveals nondeuterated (cyan channel) and deuterated (red channel) components. (c) CARS image probes C-D vibrations at 2073 cm^{-1}. (d) The Raman spectrum represents nucleoli of Raman image (a). For clarity, only nucleic acids bands are labeled. Bar=5 μm.

times—even at video time frame rates—and the use of lower incident power may reduce sample damage. The higher frequency of CARS signals allows easy separation from fluorescence background. A current drawback of CARS compared to spontaneous Raman spectroscopy is its more difficult implementation and the presence of a nonresonant background that distorts line shapes and reduces chemical contrast. Recently, a systematic comparison was reported between coherent and spontaneous Raman signals under the conditions appropriate for biological imaging.[69] In biological imaging, local concentrations are often below the millimolar range and the high power (P) is necessary for CARS enhancement owing to the quadratic dependence of CARS on the number of molecules (N) as opposed to the linear dependence of spontaneous Raman spectroscopy. It was shown that most of the values for N and P where coherent methods have a significant advantage are inaccessible in biological samples owing to photodamage or the requirements of high concentration. This result does not apply to heterodyne-detected or stimulated Raman scattering signals that scale differently with N and P. The requirement of high concentration is demonstrated in Figs. 2 and 5 and in much of the CARS imaging literature by the fact that CARS images were collected for CH and CD stretch vibrations that are the most plentiful components of lipid droplets.[4]

In summary, at low concentrations and low power, spontaneous Raman spectroscopy offers the advantage of sensitivity and also provides high resolution broadband spectra. Furthermore, spontaneous Raman spectroscopy can be done with inexpensive lasers and optics compared to the complicated parametric sources and—in case of SRS—costly electro-optic modulators. Optical sectioning can be achieved using confocal microscopes. Novel optical devices such as narrowband filters with optimized transmission and more sensitive detectors such as avalanche photodiodes or electron-multiplying CCDs might pave the way for faster, future Raman imaging at single mode or few modes in less than a minute or even seconds. The benefits of each method should be critically examined to make an optimum choice of technique.

9 Conclusion and Outlook

A tutorial of fundamentals and an overview of Raman and CARS microscopy in the field of biomedical applications has been given. Particular emphasize was put on the introduction to a versatile nonlinear variant of Raman scattering, i.e., coherent anti-Stokes Raman scattering. After describing the basic concepts of linear Raman scattering, the vibrational modes of biomolecules, and coherent Raman scattering, tissue characterization for medical diagnostics, the design of Raman/CARS-fiber probes, and investigations of the biophysics of individual cells have been discussed illustrating the great capability of Raman and CARS in life science and medicine. Further application fields of Raman and CARS microspectroscopy are expected to arise from technical innovations and advanced algorithms for data processing. This was exemplified by the combination of Raman and CARS microscopy with optical traps and microfluidics. Whereas compact and mobile Raman systems have already been introduced, the laser sources for CARS are still large, complex, and expensive. The development of new laser-sources such as tunable, femtosecond fiber lasers[38,39,48–50] are key elements to boost the applicability of nonlinear, Raman imaging and lead to further dissemination of the technique.

References

1. C. Krafft, B. Dietzek, and J. Popp, "Raman and CARS microspectroscopy of cells and tissues," *Analyst* **134**(6), 1046–1057 (2009).
2. Y. Zhang, H. Hong, and W. Cai, "Imaging with Raman spectroscopy," *Curr. Pharm. Biotechnol.* **11**(6), 654–661 (2010).
3. A. Downes and A. Elfick, "Raman spectroscopy and related techniques in biomedicine," *Sensors* **10**(3), 1871–1889 (2010).
4. J. P. Pezacki et al., "Chemical contrast for imaging living systems: molecular vibrations drive CARS microscopy," *Nat. Chem. Biol.* **7**(3), 137–145 (2011).
5. C. L. Evans and X. S. Xie, "Coherent anti-Stokes Raman scattering microscopy: chemical imaging for biology and medicine," *Annu. Rev. Anal. Chem.* **1**, 883–909 (2008).
6. W. Min et al., "Coherent nonlinear optical imaging: beyond fluorescence microscopy," *Annu. Rev. Anal. Chem.* **62**, 507–530 (2011).
7. M. Müller and A. Zumbusch, "Coherent anti-Stokes Raman scattering microscopy," *ChemPhysChem* **8**(15), 2156–2170 (2007).
8. A. Volkmer, "Vibrational imaging and microspectroscopies based on coherent anti-Stokes Raman scattering microscopy," *J. Phys. D: Appl. Phys.* **38**(5), R59–R81 (2005).
9. B. Schrader, *Infrared and Raman Spectroscopy*, VCH Wiley, Weinheim, Germany (1995).
10. S. Mukamel, *Principles of Nonlinear Optical Spectroscopy*, Oxford University Press, Oxford (1995).
11. J. De Gelder et al., "Reference database of Raman spectra of biological molecules," *J. Raman Spectrosc.* **38**(9), 1133–1147 (2007).
12. M. Schmitt, T. Mayerhöfer, and J. Popp, "Light matter interaction," in *Handbook of Biophotonics*, J. Popp, V. V. Tuchin, and S. H. Heinemann, Eds., Wiley VCH, Weinheim, Germany (2011).
13. D. A. Long and W. Kiefer, *Non-Linear Raman Spectroscopy and its Chemical Applications*, Springer, Dordrecht, The Netherlands (1982).
14. S. Begin et al., "In vivo optical monitoring of tissue pathologies and diseases with vibrational contrast," *J. Biophoton.* **2**(11), 632–642 (2009).
15. E. M. Vartiainen et al., "Direct extraction of Raman line-shapes from congested CARS spectra," *Opt. Express* **14**(8), 3622–3630 (2006).
16. Y. Liu, Y. J. Lee, and M. T. Cicerone, "Fast extraction of resonant vibrational response from CARS spectra with arbitrary nonresonant background," *J. Raman Spectrosc.* **40**(7), 726–731 (2009).
17. Y. Liu, Y. J. Lee, and M. T. Cicerone, "Broadband CARS spectral phase retrieval using a time-domain Kramers-Kronig transform," *Opt. Lett.* **34**(9), 1363–1365 (2009).
18. M. D. Duncan, "Molecular discrimination and contrast enhancement using a scanning coherent anti-Stokes Raman microscope," *Opt. Commun.* **50**(5), 307–312 (1984).
19. M. D. Duncan, J. Reintjes, and T. J. Manuccia, "Scanning coherent anti-Stokes Raman microscope," *Opt. Lett.* **7**(8), 350–352 (1982).
20. M. D. Duncan, J. Reintjes, and T. J. Manuccia, "Imaging biological compounds using the coherent anti-Stokes Raman-scattering microscope," *Opt. Eng.* **24**(2), 352–355 (1985).
21. A. Zumbusch, G. R. Holtom, and X. S. Xie, "Three-dimensional vibrational imaging by coherent anti-Stokes Raman scattering," *Phys. Rev. Lett.* **82**(20), 4142–4145 (1999).
22. J. X. Cheng et al., "An epi-detected coherent anti-Stokes Raman scattering (e-cars) microscope with high spectral resolution and high sensitivity," *J. Phys. Chem. B* **105**(7), 1277–1280 (2001).
23. A. Volkmer, J. X. Cheng, and X. S. Xie, "Vibrational imaging with high sensitivity via epidetected coherent anti-Stokes Raman scattering microscopy," *Phys. Rev. Lett.* **87**(2), 023901–023904 (2001).
24. J. X. Cheng et al., "Laser-scanning coherent anti-Stokes Raman scattering microscopy and applications to cell biology," *Biophys. J.* **83**(1), 502–509 (2002).
25. C. Krafft et al., "A comparative Raman and cars imaging study of colon tissue," *J. Biophoton.* **2**(5), 303–312 (2009).
26. M. N. Slipchenko et al., "High-speed vibrational imaging and spectral analysis of lipid bodies by compound Raman microscopy," *J. Phys. Chem. B* **113**(21), 7681–7686 (2009).
27. E. O. Potma, C. L. Evans, and X. S. Xie, "Heterodyne coherent anti-Stokes Raman scattering (cars) imaging," *Opt. Lett.* **31**(2), 241–243 (2006).

28. M. Jurna et al., "Background free cars imaging by phase sensitive heterodyne cars," *Opt. Express* **16**(20), 15863–15869 (2008).

29. J. X. Cheng, L. D. Book, and X. S. Xie, "Polarization coherent anti-Stokes Raman scattering microscopy," *Opt. Lett.* **26**(17), 1341–1343 (2001).

30. F. Ganikhanov et al., "High-sensitivity vibrational imaging with frequency modulation coherent anti-Stokes Raman scattering (fm cars) microscopy," *Opt. Lett.* **31**(12), 1872–1874 (2006).

31. N. Vogler et al., "Separation of cars image contributions with a Gaussian mixture model," *J. Opt. Soc. Am. A Opt. Image. Sci. Vis.* **27**(6), 1361–1371 (2010).

32. S. H. Parekh et al., "Label-free cellular imaging by broadband coherent anti-stokes Raman scattering microscopy," *Biophys. J.* **99**(8), 2695–2704 (2010).

33. H. A. Rinia et al., "Quantitative label-free imaging of lipid composition and packing of individual cellular lipid droplets using multiplex cars microscopy," *Biophys. J.* **95**(10), 4908–4914 (2008).

34. J. X. Cheng et al., "Multiplex coherent anti-Stokes Raman scattering microspectroscopy and study of lipid vesicles," *J. Phys. Chem. B* **106**(34), 8493–8498 (2002).

35. M. Muller and J. M. Schins, "Imaging the thermodynamic state of lipid membranes with multiplex cars microscopy," *J. Phys. Chem. B* **106**(14), 3715–3723 (2002).

36. C. L. Evans et al., "Chemical imaging of tissue in vivo with video-rate coherent anti-Stokes Raman scattering microscopy," *Proc. Natl. Acad. Sci. U. S. A.* **102**(46), 16807–16812 (2005).

37. H. Wang et al., "Coherent anti-stokes Raman scattering imaging of axonal myelin in live spinal tissues," *Biophys. J.* **89**(1), 581–591 (2005).

38. S. Begin et al., "Coherent anti-Stokes Raman scattering hyperspectral tissue imaging with a wavelength-swept system," *Biomed. Opt. Express* **2**(5), 1296–1306 (2011).

39. A. F. Pegoraro et al., "Optimally chirped multimodal cars microscopy based on a single Ti: sapphire oscillator," *Opt. Express* **17**(4), 2984–2996 (2009).

40. T. Hellerer, A. Enejder, and A. Zumbusch, "Spectral focusing: high spectral resolution spectroscopy with broad-bandwidth laser pulses," *Appl. Phys. Lett.* **85**(1), 25–27 (2004).

41. D. Zhang, M. N. Sipchenko, and J.-X. Cheng, "Highly sensitive vibrational imaging by femtosecond pulse stimulated Raman loss," *J. Phys. Chem. Lett.* **2**(11), 1248–1253 (2011).

42. B. G. Saar et al., "Video-rate molecular imaging in vivo with stimulated Raman scattering," *Science* **330**(6009), 1368–1370 (2010).

43. P. Nandakumar, A. Kovalev, and A. Volkmer, "Vibrational imaging based on stimulated Raman scattering microscopy," *New J. Phys.* **11**(3), 033026 (2009).

44. C. W. Freudiger et al., "Label-free biomedical imaging with high sensitivity by stimulated Raman scattering microscopy," *Science* **322**(5909), 1857–1861 (2008).

45. E. Ploetz, B. Marx, and P. Gilch, "Disturbing interference patterns in femtosecond stimulated Raman microscopy," *J. Raman Spectrosc.* **41**(6), 609–613 (2010).

46. C. W. Freudiger et al., "Highly specific label-free molecular imaging with spectrally tailored excitation-stimulated Raman scattering (STE-SRS) microscopy," *Nat. Photon.* **5**(2), 103–109 (2011).

47. Y. J. Lee et al., "Optimized continuum from a photonic crystal fiber for broadband time-resolved coherent anti-Stokes Raman scattering," *Opt. Express* **18**(5), 4371–4379 (2010).

48. R. Selm et al.., "Ultrabroadband background-free coherent anti-Stokes Raman scattering microscopy based on a compact Er:fiber laser system," *Opt. Lett.* **35**(19), 3282–3284 (2010).

49. A. F. Pegoraro et al.., "All-fiber cars microscopy of live cells," *Opt. Express* **17**(23), 20700–20706 (2009).

50. A. F. Pegoraro et al., "Single laser source for multimodal coherent anti-Stokes Raman scattering microscopy," *Appl. Opt.* **49**(25), F10–F17 (2010).

51. M. Miljkovic et al., "Label-free imaging of human cells: algorithms for image reconstruction of Raman hyperspectral datasets," *Analyst* **135**(8), 2002–2013 (2010).

52. M. Hedegaard et al., "Spectral unmixing and clustering algorithms for assessment of single cells by Raman microscopic imaging," *Theor. Chem. Acc.* **130**(4–6), 1249–1260 (2011).

53. T. Meyer et al., "Nonlinear microscopy, infrared, and Raman microspectroscopy for brain tumor analysis," *J. Biomed. Opt.* **16**(2), 021113 (2011).

54. N. Vogler et al., "Multimodal imaging to study the morphochemistry of basal cell carcinoma," *J. Biophoton.* **3**(10–11), 728–736 (2010).

55. L. F. Santos et al. "Fiber-optic probes for in vivo Raman spectroscopy in the high-wavenumber region," *Anal. Chem.* **77**(20), 6747–6752 (2005).

56. M. Kirsch et al., "Raman spectroscopic imaging for in vivo detection of cerebral brain metastases," *Anal. Bioanal. Chem.* **398**(4), 1707–1713 (2010).

57. M. G. Shim et al., "Study of fiber-optic probes for in vivo medical Raman spectroscopy," *Appl. Spectrosc.* **53**(6), 619–627 (1999).

58. P. Crow et al., "Assessment of fiber-optic near infrared Raman spectroscopy for diagnosis of bladder and prostate cancer," *Urology* **65**(6), 1126–1130 (2005).

59. S. W. van de Poll et al., "On-line detection of cholesterol and calcification by catheter based Raman spectroscopy in human atherosclerotic plaque ex vivo," *Heart* **89**(9), 1078–1082 (2003).

60. S. Murugkar et al., "Miniaturized multimodal CARS microscope based on MEMS scanning and a single laser source," *Opt. Express* **18**(23), 23796–23804 (2010).

61. F. Legare et al., "Towards cars endoscopy," *Opt. Express* **14**(10), 4427–4432 (2006).

62. M. Balu et al., "Fiber delivered probe for efficient cars imaging of tissues," *Opt. Express* **18**(3), 2380–2388 (2010).

63. B. G. Saar et al., "Coherent Raman scanning fiber endoscopy," *Opt. Lett.* **36**(13), 2396–2398 (2011).

64. C. Petibois, "Imaging methods for elemental, chemical, molecular, and morphological analyses of single cells," *Anal. Bioanal. Chem.* **397**(6), 2051–2065 (2010).

65. C. Krafft et al., "Near infrared Raman spectra of human brain lipids," *Spectrochim. Acta A* **61**(7), 1529–1535 (2005).

66. T. T. Le, S. Yue, and J. X. Cheng, "Shedding new light on lipid biology with coherent anti-Stokes Raman scattering microscopy," *J. Lipid Res.* **51**(11), 3091–3102 (2010).

67. S. Dochow et al., "Tumour cell identification by means of Raman spectroscopy in combination with optical traps and microfluidic environments," *Lab. Chip.* **11**(8), 1484–1490 (2011).

68. H. W. Wang et al., "Microfluidic CARS cytometry," *Opt. Express* **16**(8), 5782–5789 (2008).

69. M. Cui, B. R. Bachler, and J. P. Ogilvie, "Comparing coherent and spontaneous Raman scattering under biological imaging conditions," *Opt. Lett.* **34**(6), 773–775 (2009).